Spontaneous wave generation at strongly strained density fronts

Callum J. Shakespeare and John R. Taylor*

Department of Applied Mathematics and Theoretical Physics, University of Cambridge, Centre for Mathematical Sciences,

Wilberforce Road, Cambridge CB3 0WA, UK

**Corresponding author address:* John R. Taylor, Department of Applied Mathematics and Theoretical Physics, University of Cambridge, Centre for Mathematical Sciences, Wilberforce Road, Cambridge CB3 0WA, UK

E-mail: J.R.Taylor@damtp.cam.ac.uk

ABSTRACT

A simple analytical model is presented describing the spontaneous generation of inertia-gravity waves at density fronts subjected to strong horizontal strain rates. The model considers fronts of arbitrary horizontal and vertical structure in a semi-infinite domain, with a single boundary at the ocean surface. Waves are generated due to the acceleration of the steady uniform strain flow around the density front, analogous to the generation of lee waves via flow over a topographic ridge. Significant wave generation only occurs for sufficiently strong strain rates, $\alpha > 0.2f$, and sharp fronts, $H/L > 0.5f/N$. The frequencies of the generated waves are entirely determined by the strain rate. The lowest frequency wave predicted to be generated via this mechanism has a Lagrangian frequency $\omega = 1.93f$ as measured in a reference frame moving with the background strain flow. The model is intended as a first-order description of wave generation at submescoscale (1 to 10km wide) fronts where large strain rates are commonplace. The analytical model compares well with fully non-linear numerical simulations of the submesoscale regime.

1. Introduction

Recent observations and numerical simulations show significant inertia-gravity wave generation at density fronts (e.g. Alford et al. 2013; Danioux et al. 2012). Density fronts are regions of large horizontal density gradient, and are commonplace near the ocean surface. Wave generation at these fronts is a potential mechanism for the transfer of energy from large-scale balanced flow to waves, and from the surface into the deep ocean. Once in the ocean interior, these waves contribute to the internal wave field which includes large contributions from wind and tides. Some of this internal wave energy may be reabsorbed into the large-scale flow via wave-mean interactions (Booker and Bretherton 1967; Nagai et al. 2015). The remaining internal waves from all sources are ultimately dissipated via breaking in the ocean interior, driving turbulence and mixing, and thus contributing to the maintenance of the global overturning circulation (Polzin and Lvov 2011; Wunsch and Ferrari 2004).

The generation of waves at density fronts occurs through a variety of mechanisms including baroclinic instability of the front (e.g. Zhang 2004; Viudez and Dritschel 2006), non-linear processes at very sharp fronts (e.g. Snyder et al. 1993; Ford 1994), and forcing (e.g. from surface wind stresses or buoyancy fluxes) that varies rapidly in time (e.g. Snyder et al. 1993; Griffiths and Reeder 1996; Rossby 1938; Gill 1984; Blumen 2000) — for a detailed discussion of these and other wave generation processes the reader is referred to the review articles of Plougonven and Zhang (2014) and Vanneste (2013). Here we investigate the specific case of wave generation at fronts subject to strong confluent strain flows, defined by strain rates $\alpha \sim f$. In the present work, we will use the term 'strain rate' to describe the cross-frontal confluence — that is, $\alpha \equiv -\partial_x u$ for a front oriented along the y-axis — and not the (larger) modulus of the strain rate tensor, which we will call the 'net strain rate'. The straining is considered to arise from a larger scale background

flow — for example, an eddy field — which then acts on the relatively smaller scale front. A front in such a confluent strain field will sharpen with time in a process known as *frontogenesis* (Hoskins and Bretherton 1972). Recent observations (e.g. Shcherbina et al. 2013; Hosegood et al. 2013; Rudnick and Luyten 1996; D'Asaro et al. 2011) and numerical simulations (e.g. Rosso et al. 2015; Capet et al. 2008; Gula et al. 2014; Mahadevan and Tandon 2006) have shown that large strain rates are commonplace on the ocean submesoscale, which is characterized by horizontal scales of 1 to $10km$ (see also the review article of Thomas et al. 2008). For example, Rosso et al. (2015) observe large-scale (mesoscale) net strain rates of up to $0.4f$ in their submesoscale resolving numerical model, and show that the vertical velocity on the submesoscale is strongly correlated with the mesoscale strain rate, suggesting active submesoscale frontogenesis is present. Shcherbina et al. (2013) observe very large net strains — in places exceeding $2f$ — although this figure is the net strain rate, including the self-strain associated with the submesoscale fronts (and other phenomena). Nonetheless, collectively these studies emphasize that both sharp density fronts and large strain rates are ubiquitous at small scales in the ocean surface layer. Here we develop a simple model that predicts significant wave generation at such strained fronts.

The classical quasi- and semi-geostrophic balance frontogenesis models (Williams and Plotkin 1968; Hoskins and Bretherton 1972) assume that the strain rate is small, typically $\alpha \sim 0.1f$. In this limit, the frontal system remains close to geostrophic balance and no wave generation occurs. Wave generation at more strongly strained fronts has recently been investigated analytically by Shakespeare and Taylor (2013, 2014) and Shakespeare (2015a), motivated in-part by earlier numerical results (e.g. Snyder et al. 1993). These studies investigated the idealized problem of a uniform potential vorticity fluid with rigid lids at the top and bottom of the domain, and fronts on both boundaries. Shakespeare and Taylor (2013) examined the generation of waves in this configuration due to the adjustment of unbalanced initial conditions for weakly strained fronts.

Shakespeare and Taylor (2014) examined the same configuration, but for larger strain rates, and showed that waves are spontaneously generated as the surface front sharpens. The waves did not propagate vertically, owing to the presence of the rigid lids, and were also trapped horizontally by the confluent strain flow. The amplitude of the generated waves was found to be exponentially small for small strain rate, but substantial for larger strain rates. Shakespeare and Taylor (2015) confirmed these results by direct comparison with numerical simulations.

Here we introduce a model with two important differences to these previous models of strained internal fronts (Hoskins and Bretherton 1972; Shakespeare and Taylor 2013, 2014; Shakespeare 2015a). Firstly, we consider a semi-infinite domain with a single boundary at the ocean surface. This is more readily applicable to the ocean than previous rigid lid models, and in particular, permits the downward propagation of waves generated at the surface front. Secondly, we allow non-uniform potential vorticity, which permits surface intensified fronts where the horizontal density gradient is maximum near the surface and decays with depth, as is typically the case for ocean fronts. To make the model analytically tractable, we linearize the equations of motion. The linearized equations are only strictly valid in the limit of small geostrophic Rossby number, $Ro_g = \Delta b H/(f^2 L^2)$, where Δb is the buoyancy difference across the front, H the frontal height and L the width. This assumption is unlikely to be valid for submesoscale fronts, where Ro_g is often order one (e.g. Shcherbina et al. 2013). However, comparison of the analytical model with a fully non-linear simulation of a submesoscale front (see §3) demonstrates that the analytic model is valid at depth, away from the surface front, and in particular, accurately describes the wave field. In other words, the dynamics of waves in the far field are largely unaffected by the locally large Rossby numbers and associated non-linear dynamics at the front itself (a result also noted by Shakespeare and Taylor 2015; Shakespeare 2015a).

One objective of this paper is to investigate the dynamical mechanism responsible for the generation of waves at strained fronts. In §2b we demonstrate the mathematical similarity of the present frontal wave problem to the classical rotating lee wave problem of Queney (1947). In the Queney (1947) model waves are generated when a uniform background flow passes over a topographic ridge. The background flow is accelerated around the ridge, into the stratified ambient, and for sufficiently sharp ridges (small width L) and strong flow (large $\bar{U}$) characterized by large Rossby number $Ro = \bar{U}/(fL)$, buoyancy forces give rise to a wave response (Queney 1947; Pierrehumbert 1984; Muraki 2011). Here we show that a density front presents an obstacle to a background strain flow, in the same way a topographic ridge presents an obstacle to a uniform background flow. The background strain flow is accelerated around the density front into the stratified ambient, and for sufficiently sharp fronts and strong strain flows, buoyancy forces drive a wave response. Just like steady lee waves, these 'frontal waves' are trapped by the background flow in a distinctive pattern. The effect of a background strain flow on inertia-gravity waves has previously been considered by Plougonven and Snyder (2005) and Thomas (2012), among others; the difference here is that the strain field is responsible for both the generation and the trapping of the waves.

The paper is set out as follows. In §2 we derive the general linearized equation for the buoyancy field in a strained, quasi-two-dimensional flow. In §2a1 we write down the analytic solution for the special case of constant strain rate and stratification. The frequencies and amplitudes of generated waves can be determined directly from this solution, independent of the details of the frontal structure. We then explore the dependence of the wave generation on the strain rate (§2a2) and width of the surface front (§2a3). The dynamics of wave generation at internal fronts is compared to that at topographic obstacles in §2b. In §3 we compare the analytical model predictions with fully non-linear simulations of a submesoscale front. Lastly, in §4 we discuss the implications of these results for the generation of inertia-gravity waves in the ocean.

2. Theory

We begin our analysis with the incompressible, hydrostatic, Boussinesq equations for a rotating fluid in Cartesian coordinates. Here, we will use (U,V,W) to denote the velocity components in the (x,y,z) directions, respectively, B the buoyancy, P the pressure, and f the (constant) Coriolis frequency. The variables are decomposed into background (denoted by an overbar) and perturbation (denoted by lower case) components. The background state is one of uniform horizontal strain rate, $\bar{U} = -\alpha x$ and $\bar{V} = \alpha y$ where α may be a function of time, and background stratification, $N^2(z)$, such that $\bar{B} = \int N^2(z)\,dz$. The perturbation to this background state, or frontal anomaly — which includes the front, cross-frontal circulation and any internal wave field — is assumed to be infinitely long and oriented along the y-axis such that the perturbation flow has no y dependence. With these assumptions the flow may be written as

$$U = \bar{U} + u(x,z,t),\ V = \bar{V} + v(x,z,t),\ W = w(x,z,t) \tag{1a}$$

$$P = \bar{P} + p(x,z,t),\ b = \bar{B} + b(x,z,t), \tag{1b}$$

where the background pressure must be chosen as

$$\bar{P} = -\rho_0 \left(\frac{\alpha^2}{2}(x^2+y^2) + \frac{\partial_t \alpha}{2}(y^2-x^2) - \alpha f x y - \int \bar{B}\,dz \right), \tag{2}$$

such that the background state independently (i.e. when the perturbation variables are identically zero) satisfies the inviscid Boussinesq equations. Substituting the net fields (1) into the Boussinesq equations and simplifying yields the governing equations for the two-dimensional perturbation

fields,

$$Du = fv + \alpha u - \frac{1}{\rho_0}\frac{\partial p}{\partial x} + \nu_h \frac{\partial^2 u}{\partial x^2}, \tag{3a}$$

$$Dv = -fu - \alpha v + \nu_h \frac{\partial^2 v}{\partial x^2}, \tag{3b}$$

$$0 = -\frac{1}{\rho_0}\frac{\partial p}{\partial z} + b, \tag{3c}$$

$$Db = -N^2(z)\, w + \kappa_h \frac{\partial^2 v}{\partial x^2}, \tag{3d}$$

$$0 = \frac{\partial u}{\partial x} + \frac{\partial w}{\partial z}, \tag{3e}$$

where $D \equiv \partial_t + (u + \bar{U})\,\partial_x + w\,\partial_z$ is the material derivative. The κ_h and ν_h are the artificial horizontal diffusivity and viscosity that will be used for the numerical solutions in §3. The equations (3) are identical to those examined by previous authors (for example, the numerical study of Snyder et al. 1993, their equation 2; the only difference being that here we have the additional assumptions of incompressibility and hydrostatic balance). The five equations for the perturbation fields (3) involve five independent variables: u, v, w, p, b.

For the analytic model, we consider the inviscid case ($\kappa_h = \nu_h = 0$) and make a number of simplifying assumptions. The objective is to formulate the simplest possible model for wave generation at fronts. With that aim, here we consider the situation where the perturbation flow, u, is small compared with the background strain flow, $u \ll \bar{U}$, such that equations (3) become linear (following Shakespeare 2015a), with the material derivative only involving advection by the background flow, $D \equiv \bar{D} = \partial_t + \bar{U}\,\partial_x$. For an inviscid, weakly strained front, this assumption is equivalent to the usual quasi-geostrophic (QG) approximation that the Rossby number is small. Assuming that time scales with the inverse strain rate or *advective timescale*, $1/\partial_x \bar{U} = 1/\alpha$, and that the strain rate is small relative to the Coriolis frequency, $\alpha << f$, (3a) implies that the along-front velocity v scales geostrophically, $v \sim \Delta b H/(fL)$, while (3b) implies that $u \sim \alpha/f\, v$. For

the linear model to be strictly valid we require $u \ll \bar{U}$, or substituting the derived scales, $Ro_g = \Delta bH/(f^2L^2) \ll 1$. However, unlike previous linear QG models (e.g. Williams and Plotkin 1968), we make no assumption about the strain rate α in comparison to the inertial frequency f.

It is easily shown from the linearized equations (3) that the perturbation potential vorticity (PV) is conserved, or

$$\bar{D}q = 0, \text{ where } q = fN^2(z)\frac{\partial}{\partial z}\left(\frac{b}{N^2(z)}\right) + N^2(z)\frac{\partial v}{\partial x}. \tag{4}$$

Equation (4) implies that the PV evolves according to $\partial_t q - \alpha x \partial_x q = 0$, or that $q = q_0(xe^{\beta(t)}, z)$, where $q_0(x,z)$ is the initial PV distribution and β is the non-dimensional strain, $\beta(t) = \int_0^t \alpha(t')\,dt'$. Thus, the action of the strain flow is to squeeze a PV anomaly with time. Usually such a PV anomaly will be associated with a density front. For consistency with previous work (Shakespeare and Taylor 2013, 2014, 2015; Shakespeare 2015a), here we define the frontal buoyancy anomaly associated with the PV as

$$b_0(x,z) = \frac{N^2(z)}{f}\int_{-\infty}^{z} \frac{q_0(x,z')}{N^2(z')}\,dz', \tag{5}$$

such that the net perturbation buoyancy field, b, is

$$b(x,z,t) = b_0(xe^{\beta}, z) + b'(x,z,t), \tag{6}$$

where b' is the buoyancy response to the imposed PV anomaly. The above definition of b_0 (5) is an entirely arbitrary — but mathematically convenient — subdivision of the perturbation buoyancy b in an 'imposed anomaly' b_0 and 'response' b' and implies no additional assumptions about the flow. The objective now is to formulate an equation for the evolution of b' forced by the strain-driven sharpening of the frontal anomaly b_0.

The buoyancy response b' may be related to the along-front velocity, v, by substitution of (6) into the PV equation (4):

$$\frac{\partial v}{\partial x} = -f\frac{\partial}{\partial z}\left(\frac{b'}{N^2(z)}\right). \tag{7}$$

The solution proceeds by taking the material derivative of the y-momentum equation (3b), and substituting the x-momentum equation (3a), to obtain

$$\left(\bar{D}^2 + f^2 - \alpha^2 + \partial_t \alpha\right) v = \frac{f}{\rho_0}\frac{\partial p}{\partial x}. \tag{8}$$

We now take an x and z derivative of (8), and substitute $\partial_x v$ from (7) and $\partial_z p$ from (3c), yielding an equation for b':

$$\left(\bar{D}^2 - 2\alpha\bar{D} + f^2\right)\frac{\partial^2}{\partial z^2}\left(\frac{b'}{N^2(z)}\right) + \frac{\partial^2 b'}{\partial x^2} = -\frac{\partial^2}{\partial x^2} b_0\left(x e^{\beta}, z\right). \tag{9}$$

Equation (9) may be solved numerically for a given choice of initial conditions, buoyancy anomaly b_0, strain rate $\alpha(t)$, and stratification $N^2(z)$. In the next section we derive an analytic solution for the special case of constant strain rate and stratification.

a. Constant strain rate and stratification

Here we will first consider an infinite domain in both x and z. As will be described below, the semi-infinite domain solution with a rigid lid at $z = 0$ may be obtained directly from the infinite domain solution. Taking the Fourier transform of (9) in x and z (with N^2 and α constant) yields

$$\left[\left(\widehat{\bar{D}}^2 - 2\alpha\widehat{\bar{D}} + f^2\right)\frac{-m^2}{N^2} - k^2\right]\widehat{b'} = k^2 e^{-\alpha t}\,\widehat{b_0}\left(k e^{-\alpha t}, m\right), \tag{10}$$

where k and m are the horizontal and vertical wavenumbers, respectively, hats denote the Fourier transform, and $\widehat{\bar{D}} = \partial_t + \alpha(1 + k\partial_k)$ is the transformed material derivative. The general solution (Shakespeare 2015b, §6.2.1) to the PDE (10) for $\{\alpha, m, N\} \neq 0$ is

$$\begin{aligned}\widehat{b'}(k,m,t) = &\underbrace{-\varepsilon^2\left(G(\varepsilon)\left[e^{-\alpha t}\,\widehat{b_0}\left(k e^{-\alpha t}, m\right)\right]\right.}_{\text{forced}} \\ &\underbrace{\left. + H_+(\varepsilon)\left[e^{-\alpha t}\,c_1\left(k e^{-\alpha t}, m\right)\right] + H_-(\varepsilon)\left[e^{-\alpha t}\,c_2\left(k e^{-\alpha t}, m\right)\right]\right)}_{\text{adjustment waves}},\end{aligned} \tag{11}$$

where $\varepsilon = Nk/(fm)$, and the c_i are unknown functions dependent on the choice of initial conditions.[1] The solution (11) contains two parts. The 'forced' part is defined by the requirement that time dependence only arises through the strain-driven sharpening of the buoyancy (and PV) anomaly, $b_0(xe^{\alpha t}, z)$, as per the forcing to the right-hand side of (9) and (10). The remaining 'adjustment wave' part of (11) describes propagating waves generated due to the adjustment of initial conditions that differ from those implied by the forced solution, analogous to the waves generated during geostrophic adjustment. The unusual form of the wave solutions in (11) is due to the fact that the strain field modifies the propagation of, and ultimately traps the waves — these dynamics were studied in a similar context in Shakespeare and Taylor (2013, see section 4.2 and figure 15 therein). In the present work, our focus is on waves generated in response to strain forcing rather than via adjustment of initial conditions, and thus here we will only consider the forced part of the flow.

The functions G and $H_\pm$ in (11) are obtained by substitution of (11) into the PDE (10), yielding the ODE:

$$\left[\varepsilon^2\delta^2\frac{\partial^2}{\partial\varepsilon^2} + 3\delta^2\varepsilon\frac{\partial}{\partial\varepsilon} + 1 + \varepsilon^2\right] G(\varepsilon) = -1, \tag{12}$$

where $\delta = \alpha/f$ is the non-dimensional strain rate (also called the 'strain Rossby number'). The particular and homogeneous solutions to (12) are, respectively,

$$G(\varepsilon) = -1 + \frac{\varepsilon^2}{1+8\delta^2}\,{}_1F_2\left(1; \left(\frac{5}{2} - \frac{\imath\sigma}{2}, \frac{5}{2} + \frac{\imath\sigma}{2}\right); -\frac{\varepsilon^2}{4\delta^2}\right), \tag{13}$$

$$H_\pm(\varepsilon) = \frac{1}{\varepsilon}J_{\pm\sigma\imath}\left(\frac{\varepsilon}{\delta}\right), \tag{14}$$

where ${}_pF_q$ is the generalized hypergeometric function, J is the Bessel function of complex order, and $\sigma = \sqrt{(f/\alpha)^2 - 1}$. The choice of the particular solution to (12), $G(\varepsilon)$, is unique in that it is

[1] This solution structure emerges due to the form of the material derivative in the linearized system; i.e. $\widehat{\bar{D}}\left[e^{-\alpha t}\,\widehat{F}\,(ke^{-\alpha t}, m)\right] = 0$ for any $\widehat{F}$, which is the Fourier equivalent of $\bar{D}[F(xe^{\alpha t}, z)] = 0$.

the only solution to (12) that is finite at $\varepsilon = 0$, implying that the forced solution is also unique as explained below.

1) Green's Functions

The forced part of the solution (11) can be rewritten in terms of the along-front shear, by Fourier transforming (7) to yield

$$\widehat{\partial_z v} = \imath k \widehat{b'}/(f\varepsilon^2) = f^{-1} G(\varepsilon) \left[-\imath k e^{-\alpha t} \widehat{b_0}\left(k e^{-\alpha t}, m\right)\right]. \tag{15}$$

The function $\widehat{\partial_z v}_G = f^{-1} G(\varepsilon)$ in (15), with G defined by (13), is the *Green's function* for the along-front shear. It contains all the dynamics and structure of the forced response, independent of the details of the buoyancy anomaly b_0. The Green's function depends only on the scaled wavenumber, $\varepsilon = kN/(fm)$, which can be thought of as the Burger number, or scaled slope, of a given mode (k,m). In physical space, the solution (15) may be written as a double convolution of the Green's function with the buoyancy gradient anomaly,

$$\partial_z v(x,z,t) = \int_{-\infty}^{\infty}\int_{-\infty}^{\infty} \partial_z v_G(x-x_0, z-z_0) \frac{\partial}{\partial x_0} b_0\left(x_0 e^{\alpha t}, z_0\right) dx_0\, dz_0. \tag{16}$$

A valid solution for the along-front shear requires that its integral over all x has a finite value. The integral over all x is equal to the $k = \varepsilon = 0$ value of its spectrum, $\widehat{\partial_z v}(0)$ in (15). The square bracketed factor in (15) corresponds to the buoyancy anomaly gradient. Again, the $k = \varepsilon = 0$ value of this factor is the integral over all x of the buoyancy gradient: $\int_{-\infty}^{\infty} \partial_x b_0(xe^{\alpha t}, z)\, dx = \Delta b(z)$, the buoyancy difference across the front, which is finite and invariant time. For $\widehat{\partial_z v}(0)$ to be finite we thus require that $G(0)$ is finite. The only possible solution for $G(\varepsilon)$ is therefore that defined by (13), since the $H_{\pm}(\varepsilon)$ homogeneous solutions (14) are infinite at $\varepsilon = 0$. The forced solution (15) is therefore unique and its properties controlled by the Green's function $G(\varepsilon)$ (13).

Green's functions for other fields may also be written as derivatives of $G(\varepsilon)$. For instance, since $u = -f^{-1}(\bar{D}+\alpha)v$ from (3b), it may be shown that the Green's function for the cross-front shear is defined by

$$\widehat{\partial_z u}_G = -f^{-1}\,\delta\left(\varepsilon\frac{\partial}{\partial\varepsilon}+2\right)G(\varepsilon). \tag{17}$$

Similarly, the Green's function for the divergence may be derived from continuity (3e) and satisfies,

$$\widehat{\partial_x u}_G = -\widehat{\partial_z w}_G = -N^{-1}\,\delta\,\varepsilon\left(\varepsilon\frac{\partial}{\partial\varepsilon}+2\right)G(\varepsilon). \tag{18}$$

Note that the motivation for using the shears and divergences of the velocity fields in the above expressions, rather than the velocities themselves, is that the former depend only on the scaled mode slope, $\varepsilon = Nk/(fm)$, whereas the latter depend on the individual horizontal and vertical wavenumbers.

The non-dimensional Green's function for the cross-front shear, $f\,\widehat{\partial_z u}_G$, is shown in figure 1. The behavior of the Green's function depends strongly on the magnitude of the strain rate. For small strain rates, $\delta \sim 0.1$, the function decays smoothly to zero with increasing scaled mode slope ε. For larger strain rate, $\delta \geq 0.2$, the Green's function is smoothly decreasing for small slopes $\varepsilon < 1$ but exhibits high-amplitude oscillations in the region $\varepsilon > 1$, implying the accumulation of energy at certain preferential wavenumber combinations, $\varepsilon = Nk/(fm)$, or resonant modes. As will be seen below, these oscillations correspond to a set of stationary waves with phase slopes of $k/m = f\varepsilon/N$ and Lagrangian frequencies $\omega = f\sqrt{1+\varepsilon^2}$ [2]. The logarithmic color scale in figure 1 indicates that the amplitude of the oscillations (and therefore waves) is *exponentially small* at small strain rate (consistent with the result derived in the rigid-lid case studied in Shakespeare and Taylor 2014).

[2]Here, the Lagrangian frequency denotes the frequency a wave would have if it were observed in a reference frame moving with the background flow, as opposed to the Eulerian frequency which is the frequency that is observed at a fixed point in space. This distinction will become important in subsection 4 below.

The differing behavior at small and large strain rate is captured by the two asymptotic limits. In the limit of vanishingly small strain rate, $\delta \to 0$, the Green's function asymptotes to a smoothly decaying profile,

$$G(\varepsilon) = -\frac{1}{1+\varepsilon^2}, \tag{19}$$

and corresponds to an along-front velocity in geostrophic balance with the buoyancy anomaly (i.e. the Williams and Plotkin (1968) solution). In contrast, the Green's function for large strain rate, $\delta \to \infty$, asymptotes to an oscillation-dominated profile,

$$G(\varepsilon) = -\frac{2\delta}{\varepsilon} J_1\left(\frac{\varepsilon}{\delta}\right), \tag{20}$$

where J_1 is the 1st order Bessel function.

2) Strain rate dependence

To construct the full solution from the Green's functions we require knowledge of the structure of the buoyancy gradient anomaly, $\partial_x b_0$, at some instant in time. The solution at that time is given by the convolution of the anomaly with the Green's function, as per (15) and (16). We are primarily interested in solutions in the semi-infinite domain $z \leq 0$, with a rigid-lid representing the ocean surface at $z = 0$. Here we will consider a simple surface-intensified buoyancy anomaly, or front, of the form

$$b_0(x,z) = \frac{\Delta b_0}{2} \exp\left(-\left(\frac{z}{H}\right)^2\right) \operatorname{erf}\left(\varepsilon_F \frac{x}{L_R}\right), \tag{21}$$

where H is the height scale of the front, Δb_0 is the change in buoyancy across the front and $L_R = NH/f$ is the Rossby radius. The parameter $\varepsilon_F = L_R/L$ is the Burger number, or characteristic slope, of the frontal anomaly. Solutions for the semi-infinite domain can be generated using the solutions in the previous section by mirroring the buoyancy anomaly defined for $z \leq 0$ into the region $z > 0$; that is, multiplying b_0 by $-\text{sign}(z)$.[3] This process ensures that the solution contains

[3] This is equivalent to changing the vertical Fourier transform to a sine transform.

only odd (sine) vertical modes, and thus enforces the rigid-lid boundary condition of $w = 0$ at $z = 0$.

The vertical velocity fields for a frontal Burger number (ε_F) of 1 and strain rates of (a) $0.1f$, (b) $0.3f$ and (c) $1.0f$ are shown in figure 2. For the small strain rate case ($\alpha = 0.1f$, figure 2a) the velocity is dominated by an ascending vertical jet on the warmer (right-hand) side of the front, and a descending jet on the cooler side, consistent with the classical paradigm of the thermally-direct secondary circulation about a strained front. The larger strain rates show a similar circulation about the surface front, but the steepness and strength of the jets is increased. In addition the larger strain rate solutions exhibit banded structures at depth, which correspond to horizontally trapped inertia-gravity waves. The amplitude of these waves is substantially less than the secondary circulation for moderate strain rate ($\alpha = 0.3f$, figure 2b), but of similar order for large strain rate ($\alpha = 1.0f$, figure 2c). Note that the amplitude of the secondary circulation (vertical velocity magnitude) in each case can be significantly larger if non-linear effects are considered, owing to the non-linear sharpening of the surface front (see §3).

The variation with strain rate of the strength and steepness of the surface frontal jets — which are associated with a large divergence $\partial_z w$ — can be predicted directly from the divergence Green's function (18). For small strain rates, the divergence Green's function has a single extremum in ε — since there are no waves in the flow this extremum must correspond to the frontal jets (secondary circulation). As the strain rate is increased, this extremum is retained, but additional extrema begin to appear at larger ε. We interpret these additional extrema as corresponding to the resonant wave modes of the system, as will be examined in more detail below.[4] Nonetheless, for now we extract the ε for which the first extremum (in ε) in the divergence Green's function occurs at each value of

[4]However, note that uniquely defining the 'wave' flow in the present system is problematic, as has been discussed previously by Shakespeare and Taylor (2014).

strain rate. The slope of the jets, $k/m = f\varepsilon/N$, predicted by this method is indicated by grey lines in figure 2. More generally, the jet slope as a function of strain rate is shown in figure 3a. The slope is constant for small strain rate, but increases linearly at large strain rate. The asymptotic limits (indicated by dashed lines on the figure) may be derived directly from the asymptotic Green's functions. In the limit $\delta \to 0$ (19) the local maxima of the divergence Green's function is located at $\varepsilon = 1/\sqrt{3}$, implying that the jets have a slope of $k/m = f/(N\sqrt{3}) \simeq 0.58\, f/N$. In this limit, the scale of the frontal circulation is largely unaffected by the presence of the (weak) strain flow. For large strain rate, $\delta \to \infty$, (20) the jets are steeper, with slope $k/m \simeq 1.26\,\alpha/N$. In this limit, the convergent strain flow strongly confines the frontal circulation in the horizontal, leading to steeper, intensified jets.

The vertical velocity magnitude (jet strength) may also be estimated from the Green's function as the local maximum value of the divergence, and is plotted in figure 3b. The vertical velocity increases linearly at small strain rate and quadratically at large strain rate. The linear increase at small strain rate is predicted from quasi- and semigeostrophic models of frontogenesis (Williams and Plotkin 1968; Hoskins and Bretherton 1972) and is merely a requirement of continuity: a larger background strain flow implies a correspondingly larger secondary circulation to conserve volume at the front, since a greater volume of fluid must be deflected down and around the frontal anomaly. The additional (quadratic) increase in vertical velocity at large strain rate is associated with the linear increase in the slope of the jets, which is due to the strong strain flow confining the secondary circulation around the strain axis, as noted above. While non-linear effects will modify the magnitude of the secondary circulation (see §3), the confinement effect of the strain flow will still operate (as shown in the numerical simulations of Shakespeare and Taylor 2015), and thus the qualitative dependence of the secondary circulation on the strain rate described here is expected to be robust. Indeed, figure 3b is qualitatively similar to the results of Rosso et al. (2015), in particular

their figure 5b, which displays the dependence of the vertical velocity on the large-scale strain rate in their submesoscale-resolving numerical model of a sector of the Southern Ocean. The strain rate dependence of the vertical velocity predicted here may thus have application in parameterizing vertical velocities associated with fronts in ocean models of sufficiently high resolution to allow fronts to form, but with insufficient resolution to accurately model the frontal circulation.

The slopes and Lagrangian frequencies of the waves (resonant modes) as a function of strain rate can also be determined by computing the local extrema of the Green's function for the cross-frontal shear (17) shown in figure 1. This technique works since the waves visible in the solutions (e.g. figure 2) are associated with a local maximum in the cross-frontal shear, as well as the vertical velocity and divergence.[5] In figure 4 we plot the frequencies and amplitudes of the six lowest frequency resonant modes of *significant* amplitude — we cannot rule out the presence of low amplitude, lower frequency modes that are obscured by the secondary circulation and which therefore do not generate extrema in the Green's function spectrum. The Lagrangian wave frequency is related to the wave slope via $\omega = f\sqrt{1+\varepsilon^2}$. The lowest Lagrangian frequency associated with a distinct wave mode is $1.93f$ and occurs for a strain rate of approximately $0.3f$ (the strain rate used in figure 2b). For strain rates in the range $0.2f < \alpha < f$, the lowest frequency distinct mode has a Lagrangian frequency less than $4f$. The wave slopes predicted from figure 4 are indicated as grey lines on the vertical velocity plots in figure 2b,c.

3) Frontal scale dependence

In this section we address the question of how the frontal Burger number, or characteristic frontal slope, $\varepsilon_F = L_R/L = NH/(fL)$, affects the solution for a given value of strain rate. The confluent strain acts to compress the horizontal scale L of the frontal buoyancy gradient anomaly $\partial_x b_0$ with

[5] Using the Green's function for the divergence instead of the cross-frontal shear does not produce substantially different results.

time as per (16). The Burger number of the front will thus increase with time according to $\varepsilon_F = \varepsilon_{F,0}\, e^{\alpha t}$. In other words, there is a one-to-one relationship between the frontal scale and time. Thus, examining the Burger number dependence of the solution will also tell us about the time evolution of the front.

Figure 5 displays the vertical velocity fields for a front subject to a strain rate of $\alpha = 0.4f$, for five frontal scales (or time snapshots). The buoyancy anomaly is the same as used previously (21). When the frontal width is large compared to the Rossby radius (a, $L = 10L_R$; b, $L = 5L_R$), the secondary circulation is broad and relatively weak. In particular, for wide fronts ($L \gg L_R$), there are no waves present. As the frontal width approaches the Rossby radius (c, $L = 2L_R$), the lowest frequency (primary) wave mode appears. As the frontal width is reduced further (d, $L = L_R$; e, $L = 0.5L_R$), the primary wave mode amplifies and higher frequency packets appear. We observe that the slopes (indicated on the figure by dashed grey lines) of both the frontal jets and the waves are independent of the frontal width, implying that the vertical scale of the flow decreases at the same rate as the horizontal to keep the slope constant.

This behavior may be understood by considering the form of the solution (15). The solution at a given time is defined by the product of the Green's function and the buoyancy gradient anomaly spectra evaluated at that instant in time. The possible slopes of the jets and waves are controlled by the structure of the Green's function at a given value of the strain rate, whereas the amplitude of those features is controlled by the spectral amplitude of the buoyancy gradient anomaly at the corresponding wavenumber combinations. For instance, the amplitude of a wave mode with a given slope, $\varepsilon = Nk/(fm)$, is determined by the integrated amplitude in the buoyancy gradient spectrum, $\widehat{\partial_x b_0}(k,m)$, along the line $m = Nk/(f\varepsilon)$. As the frontal scale is reduced, the gradient spectrum has more amplitude at higher horizontal wavenumbers k, and therefore more amplitude at steeper slopes. Since, as shown in figure 1, wave modes are only present in the region $\varepsilon = Nk/(fm) > 1$,

the spontaneous generation of waves can only occur for fronts with significant spectral amplitude at the corresponding wavenumbers. Fronts that satisfy this requirement are characterized by order one Burger numbers, $\varepsilon_F \sim 1$. Thus, as seen in figure 5, significant spontaneous wave generation via the present mechanism is only observed for fronts with widths comparable to the Rossby radius, or smaller.

4) Ray tracing and wave trapping

Here we apply ray tracing theory to demonstrate that the resonant wave modes seen in the above solutions correspond to wave packets that are generated at (or near) the front, and are confined horizontally by the strain flow. Our analysis follows that of Reeder and Griffiths (1996) who studied a very similar strained front system but via a numerical approach. The equations governing the propagation of a wave packet in the xz plane are

$$\left(\frac{D}{Dt}\right)_g k = -\frac{\partial \Omega}{\partial x}, \tag{22a}$$

$$\left(\frac{D}{Dt}\right)_g m = -\frac{\partial \Omega}{\partial z}, \tag{22b}$$

$$\left(\frac{D}{Dt}\right)_g x = \frac{\partial \Omega}{\partial k}, \tag{22c}$$

$$\left(\frac{D}{Dt}\right)_g z = \frac{\partial \Omega}{\partial m}, \tag{22d}$$

where $(D/Dt)_g$ is the material derivative following a packet, which propagates with speed $\vec{c_g} = (\partial_k \Omega, \partial_m \Omega)$ as per (22)c,d, and Ω is the appropriately Doppler shifted (or Eulerian) frequency. For the strain flow used here the Doppler shifted frequency is

$$\Omega = \omega(k,m) - \alpha k x, \quad \text{where} \quad \omega(k,m) = \pm f \sqrt{1 + \left(\frac{Nk}{fm}\right)^2}, \tag{22e}$$

is the regular hydrostatic dispersion relation for inertia-gravity waves. We note that here, consistent with our basic model, we assume hydrostatic dynamics in our ray-tracing equations, and thus

our ray-tracing analysis is only valid for sufficiently large horizontal scales (or small times). A discussion of non-hydrostatic effects is beyond the scope of this paper and the interested reader is referred to Shakespeare (2015a). Further, (22) are only valid for fronts that of sufficiently small Rossby number (consistent with the assumptions in our theoretical treatment) such that they do not effect the wave dispersion relation; waves generated at stronger fronts may be trapped within the front (Kunze 1985; Whitt and Thomas 2013) rather than propagating away. For a detailed derivation of the above equations (22), which are identical to equations 20, and 25 through 28, of Reeder and Griffiths (1996), the reader is referred to that paper. The ray tracing equations (22) may be solved explicitly to determine the behavior of a wave packet in the flow. Supposing the packet has initial wavenumbers (k_0, m_0), (22)a,b imply that the wave numbers at some later time are

$$k = k_0\, e^{\alpha t}, \;\text{ and }\; m = m_0. \tag{23}$$

Thus, the action of the barotropic strain flow is to exponentially increase the horizontal wavenumber with time, without altering the vertical wavenumber (as described by Reeder and Griffiths 1996; Plougonven and Snyder 2005; Thomas 2012, among others). We can now substitute the above results (23) into (22)c to obtain a differential equation for the x-position of the wave packet,

$$\left(\frac{D}{Dt}\right)_g x = \pm e^{-\alpha t}\frac{\partial\omega(k_0 e^{\alpha t}, m_0)}{\partial k_0} - \alpha x \implies \left(\frac{D}{Dt}\right)_g \left(x e^{\alpha t}\right) = \pm\frac{\partial\omega(k_0 e^{\alpha t}, m_0)}{\partial k_0}. \tag{24}$$

Equation (24) may be directly integrated in time[6] to obtain

$$x = x_0 e^{-\alpha t} \pm \frac{e^{-\alpha t}}{\alpha k_0}\left(\omega(k_0 e^{\alpha t}, m_0) - \omega(k_0, m_0)\right), \tag{25a}$$

where x_0 is the initial horizontal location of the wave packet (this result was also obtained by Shakespeare 2015a, equation 15 therein). Following the same procedure for (22)d yields the z-

[6]Note that the initial wavenumbers k_0 and m_0 are constants with respect to the material derivative $(D/Dt)_g$.

position of the wave packet as a function of time

$$z = z_0 - \frac{1}{m_0 \alpha} \left(\omega(k_0 e^{\alpha t}, m_0) - \omega(k_0, m_0) \right), \tag{25b}$$

where z_0 is the initial vertical location of the wave packet. We anticipate that wave packets will be generated at the origin (where the front is located) such that $x_0 = z_0 = 0$, although the exact time of generation is unclear. Using the nomenclature of previous sections the Burger number of a given wave packet is $\varepsilon_{wp} = N k_0 e^{\alpha t}/(f m_0)$. Regardless of exactly when the wave packet is generated (25) implies that the packet will only propagate away from the origin when ε_{wp} is order one or larger, since when $\varepsilon_{wp} \ll 1$ the Lagrangian frequency $\omega(k_0 e^{\alpha t}, m_0)$ is close to inertial (and is equal to the initial frequency $\omega(k_0, m_0)$, and thus the location of the packet defined by (25) is close to zero). This result is consistent with our observation in previous sections that waves are only observed in the solution when the front is sufficiently sharp, defined by $\varepsilon \sim 1$. Furthermore, (25) shows how the packet is confined horizontally by the confluent strain flow; taking the large time limit of (25a) yields $x \to N/(\alpha m_0)$. Thus a wave packet of vertical wavenumber m_0 ultimately stagnates (horizontally) at a point in the flow where its maximum hydrostatic horizontal group speed, N/m_0, equals the strain flow speed, αx (this is only true for hydrostatic fluids; see Shakespeare 2015a). The packet is not confined vertically, and indeed the vertical position of the packet increases exponentially, $z \to -N k_0 e^{\alpha t}/(\alpha m_0^2)$ at large time (25b) as a result of the barotropic straining field.

In figure 5 we plot the path of a single wave packet, which we assume to be generated at the origin at time zero (figure 5a). We choose initial wavenumbers of $k_0 = 0.2/L_R$ and $m_0 = 0.5/H$ corresponding to an initial scale consistent with the scale of the secondary circulation in figure 5a. The path of the wave packet predicted by (25) is displayed as a solid black line on 5b to e, with the terminus of the line denoting the position of the wave packet at the time each flow

snapshot is taken. The terminus of the ray path on each plot roughly approximates the position of the deepest, gravest phase lines that appear as time increases. In other words, the chosen vertical wavenumber m_0 corresponds to the largest, and therefore fastest propagating, in the system. The ray path also approximately captures the horizontal spread of the wave energy at late time (figure 5e). As predicted by the above theory the ray asymptotes to $N/(\alpha m_0) = 5L_R$ at late time. Of course, the solution will contain waves with a range of vertical wavenumbers m_0, the spectrum of which will be set by the vertical structure of the front. Wave packets with higher m will propagate more slowly in the vertical, and be confined horizontally closer to the origin. Thus, as seen in figure 5c,d,e, these additional packets will modify the wave phase lines in that region after the fastest packet has already propagated past.

b. Comparison with rotating lee waves

It is useful to compare the present mechanism of spontaneous generation to other well known mechanisms, specifically 'lee wave' generation associated with flow across topography in a rotating system. The classical rotating lee wave model of Queney (1947) describes the steady state associated with a uniform background flow, $\bar{U} = U_0$, passing over a topographic ridge, $z = h(x)$, on an f-plane. The equation for the perturbation buoyancy, $b = B - N^2 z$, is

$$\left[\underbrace{\left(\bar{D}^2}_{accel.} + \underbrace{f^2\right) \frac{1}{N^2} \frac{\partial^2}{\partial z^2} + \frac{\partial^2}{\partial x^2}}_{geostrophic} \right] b = 0, \tag{26}$$

where $\bar{D} = U_0 \partial_x$ at steady state. The equation is composed of two parts: the usual geostrophic scaled Laplace operator familiar from classical QG models, which will yield a smooth large-scale flow, and an acceleration term associated with advection by the background flow which is responsible for the generation of small-scale stationary waves. The boundary condition on (26) is no normal flow at the ridge. Since the flow is inviscid, an equivalent condition is that the ridge

is an isopycnal surface; that is, the net buoyancy $B = b + N^2 z = 0$ at $z = h(x)$ or the perturbation buoyancy is $b(z = h(x)) = -N^2 h(x)$. In the linearized model (valid for small ridge heights) the boundary condition is applied at $z = 0$, and the solution (e.g. Queney 1947; Pierrehumbert 1984) is defined by the convolution

$$b(x,z) = -N^2 \int_{-\infty}^{\infty} G_L(x - x_0, z)\, h(x_0)\, dx_0, \tag{27}$$

where the Fourier transform of the Green's function G_L is

$$\widehat{G_L}(k,z) = \begin{cases} \exp \frac{\imath N k z}{\sqrt{k^2 U_0^2 - f^2}} & k > \frac{f}{U_0} \\ \exp \frac{-N k |z|}{\sqrt{f^2 - k^2 U_0^2}} & 0 \le k \le \frac{f}{U_0} \end{cases} . \tag{28}$$

As with the equation (26), the steady solution is thus composed of two parts: a large-scale component that decays with height, and a short-scale wave component that does not. These waves are generated when the background flow is deflected (or accelerated) sufficiently rapidly over the ridge into the stratified ambient, which provides a restoring force. Waves can only propagate for Lagrangian frequencies exceeding f and *strong* wave generation only occurs when the acceleration (or advective) timescale of $1/(kU_0)$ is of this order, $1/(kU_0) \sim 1/f$, or equivalently the Rossby number is order one, $Ro_L = U_0/(fL) \sim 1$. If the ridge is wide or the flow weak such that $Ro_L \ll 1$, then there is no significant wave field and flow remains in linearized, uniform PV geostrophic balance, defined by $\widehat{G_L}(k,z) = \exp(-Nk|z|/f)$.

Compare the 'lee wave dynamics' described in the previous paragraph, to the dynamics of the strained front considered in earlier sections. To make the analogy clearer, here we write the governing equation for a strained front with uniform interior PV ($q_0 = 0$). This equation is (9) with N^2 constant and frontal anomaly b_0 independent of z, or

$$\left[\underbrace{\left(\bar{D}^2 - 2\alpha\bar{D}\right)}_{accel.} + \underbrace{f^2 \right)\frac{1}{N^2}\frac{\partial^2}{\partial z^2} + \frac{\partial^2}{\partial x^2}}_{geostrophic} \right] b = 0, \tag{29}$$

subject to boundary condition $b = b_0\,(x e^{\alpha t})$. Equation (29) describing a strained front is identical in structure to (26) describing flow over a ridge — only the form of the acceleration terms differ. The forced solution to (29) is defined by the convolution

$$b(x,z,t) = \int_{-\infty}^{\infty} G_F(x-x_0,z)\, b_0\left(x e^{\alpha t}\right)\, dx_0, \tag{30}$$

where the Green's function G_F may be determined via Fourier inversion of the Green's function G defined in (13). Unlike lee waves, where the ridge is rigid, the front deforms (sharpens) with time as defined by the $b_0(x e^{\alpha t})$ in (30). However, the solution for a particular frontal width at some instant in time may be directly compared to the steady lee-wave solution for a ridge of the same width. As for lee waves, this solution can be considered to be composed of two parts: a large-scale secondary circulation or 'deflection' about the front, and a smaller-scale wave field. Unfortunately, unlike the lee waves, the two parts are not readily separable. As was shown in §2a2, if the strain rate $\delta = \alpha/f \ll 1$ — analogous to $Ro_L \ll 1$ for the lee waves — then there is negligible generation of waves, and the flow reduces to geostrophic balance with G defined by (19). Notably, in this small Rossby number limit, the topographic Green's function is the identical to the frontal Green's function, $\widehat{G_F} = \widehat{G_L} = \exp(-Nk|z|/f)$. Comparing (27) and (30) thus implies that the geostrophic buoyancy field associated with a topographic ridge of profile $h(x)$ is identical to the geostrophic buoyancy field associated with a front with surface buoyancy profile $b_0(x) = -N^2 h(x)$ at some instant in time. The secondary circulation around the front/ridge is determined by material conservation of the buoyancy, $w = -\bar{D}b/N^2$, and so will be different for the front and ridge owing to the different material derivative operator $\bar{D}$. However, in both cases the secondary flow is generated owing to the need for the far-field horizontal flow to be deflected along isopycnals and around the surface obstacle. If this deflection is sufficiently sharp/fast (i.e. Ro_L, δ non-small) then buoyant forces give rise to a wave response.

3. Numerical model comparison

Here we describe a solution to the fully non-linear equations (3) for parameter values representative of a submesoscale front. We consider a front with an initial structure of

$$b(x,z,0) = \frac{\Delta b}{2}\left(1+\mathrm{erf}\left(\frac{x}{L}\right)\right)\exp\left(-\left(\frac{z}{H}\right)^2\right)+N^2 z, \tag{31}$$

and choose a buoyancy difference of $\Delta b = 5\times10^{-3}\,m^2s^{-1}$, initial frontal width of $L = 10\,km$, depth scale of $H = 100\,m$, stratification $N^2 = 1\times10^{-5}\,s^{-1}$ and assume $f = 1\times10^{-4}s^{-1}$. These parameters correspond to an initial geostrophic Rossby number — the parameter assumed to be small in the linear model — of $Ro_g = \Delta bH/(f^2L^2) = 0.5$, although Ro_g increases to $O(10)$ as the front collapses. To prevent the generation of waves associated with the adjustment of unbalanced initial conditions, we initialise the numerical model with zero strain flow in a state of geostrophic balance and gradually ramp-up the strain rate with time according to $\alpha(t) = \alpha_0\left(1-\exp-(t/\tau)^2\right)$. Here we select a maximum strain rate of $\alpha_0 = 0.4f$ and ramp-up timescale of $\tau = 2\pi/f$.

The numerical model employed is MITgcm (Marshall et al. 1997) configured in hydrostatic, two-dimensional, ocean-only mode with a rigid-lid ocean surface. The MITgcm code is modified to include the background strain advection terms in (3) as an external forcing in the buoyancy and horizontal momentum equations. The domain width is chosen as $200\,km$ with the front in the centre of the domain and a horizontal resolution of $100\,m$ at the front. Open boundaries with Orlanski radiation conditions are used at the horizontal edges of the domain. The domain depth is set to $8\,km$ with resolution varying from $5\,m$ at the surface to $25\,m$ at depth. A uniform background horizontal diffusivity and viscosity of $10\,m^2s^{-1}$ is introduced to prevent the collapse of the front below the grid-scale. We also add a diffusive sponge in the deep which absorbs downward propagating waves and prevents reflections off the base of the domain. The sponge takes the form of an elevated

horizontal diffusivity and viscosity in the bottom half of the domain, $\kappa_h(z) = \kappa_\infty(1+\text{erf}(-(z+6)/1.5))/2$ where $\kappa_\infty = 400\,m^2s^{-1}$ and z is in units of kilometers.

The numerical model ultimately reaches a steady state where strain-driven sharpening of the front is balanced by the explicit horizontal diffusion. The time evolution of the model's surface buoyancy field towards this steady state is shown in figure 6. The magnitude of the strain rate as a function of time is also shown. As the front sharpens it moves to the left, with warmer fluid slumping over cooler. The front reaches a steady state after about two days with a steady cross-frontal width of about $700\,m$. The vertical velocity field in the steady state is shown in figure 7a. The grey lines on the figure are the wave and jet slopes predicted from the Green's function derived in the previous section. These predicted slopes show good agreement with the numerical solution.

For comparison, the vertical velocity field predicted from the analytical model is shown in figure 7b. This prediction is derived in the following way. First, the frontal anomaly b_0 is determined from the initial buoyancy field $b(x,z,0)$ used in the numerical model (31). This is done by replacing the velocity v in the PV relation (7) with the geostrophic velocity from (15) (since the model is initialised in geostrophic balance) and rearranging to obtain,

$$b_0 = b - b' = b + \left(\frac{N}{f}\right)^2 \int\int \frac{\partial^2 b}{\partial x^2}\, dz\, dz. \tag{32}$$

In the absence of diffusion the frontal anomaly would sharpen continuously in time according to $b_0(xe^{\beta(t)}, z)$ as discussed previously (where $\beta(t) = \int_0^t \alpha(t')\,dt'$). The inclusion of diffusion will limit the sharpening of the front to a finite width. To determine this width, consider that at steady state the dominant balance is between the strain and diffusion, or $-\alpha x \partial_x b \simeq \kappa_h \partial_{xx} b$, which may be solved to obtain $b(x) = \Delta b\,(1+\text{erf}\,(x/L_s))/2$ where the width of the front is $L_s = \sqrt{2\kappa_h/\alpha}$ (Shakespeare and Taylor 2015). For the present values the steady frontal width is $L_s = 707\,m$ in agreement with figure 6. Thus, the frontal anomaly b_0 will approach $b_0(xL_0/L_s, z)$ at large

time, where L_0 is the initial frontal width. This frontal anomaly is convolved with the Green's function to determine the analytical vertical velocity field shown in figure 7b. The waves seen in this solution compare well in both structure and amplitude with those in the numerical model solution, particularly at depth.

The region where the linear model is expected to break down may be computed by considering the linearization assumption, $|u| \ll |\bar{U}|$, made in the model derivation. The edge of this region approximately corresponds to the line along which $|u| = 0.1|\bar{U}|$ (solid black curve on figure 7) as derived from the analytic solution. Indeed, the major differences between the numerical and analytical solutions occur near the surface front within this contour, where the secondary circulation (i.e. u) and local Rossby number are large. Figure 8 shows a magnified view of the steady solutions near the surface front. The local vorticity Rossby number, $Ro = f^{-1}\partial_x v$, from the numerical model (figure 8a) peaks at a value of 7.9 at the surface front. Associated with this large Rossby number, the surface front in the numerical solution (figure 8b) has slumped to the left under the influence of gravity. This slumping has the effect of stabilizing the isopycnals compared to the analytic solution (figure 8c), which is gravitationally unstable near the surface. Associated with the non-linear leftward slumping of the front, the numerical vertical velocity (figure 8b) is weakened on the warm (cyclonic; right) side of the front, and strengthened on the cool (anticyclonic; left) side, relative to the analytic solution. The numerical solution also exhibits an intense downward jet on the cool side of the front, not present in the analytic solution. Similarly, the first few lowest Lagrangian frequency waves on the cool side of the front are intensified and steepened directly below the surface front. Furthermore, in the numerical solution the first (lowest frequency) wave mode appears on the cool side of the front around $t = 20$ hours, whereas the corresponding wave mode on the warm side of the front only appears later, around $t = 25$ hours. This behavior contrasts with the perfect antisymmetry maintained by the linearized analytic solution.

Some of the non-linear dynamics associated with the surface front in the numerical solution can be described by non-linear frontal models (e.g. Hoskins and Bretherton 1972; Shakespeare and Taylor 2014) which use the momentum coordinate, $X = x + v/f$, to include the effect of non-linear cross-frontal advection (i.e. $u\partial_x$). The buoyancy b in the non-linear models is described by the same equation as in the linear models, but in the transformed coordinate — that is, with x in (9) replaced by X (Shakespeare 2015a). In other words, non-linear models of two-dimensional fronts differ from linear models by the translation $x = X - v(X,z,t)/f$ of the solution, where X is the coordinate appearing in the linear solution. The *magnitude* of the along-front flow v does not change. However, the coordinate contraction associated with the translation $x = X - v(X,z,t)/f$ does imply an amplification of the cross-frontal flow (i.e. u, w) to conserve volume. In particular, the vertical velocity in the non-linear solution is scaled by the absolute vorticity, $\zeta/f = (1 + f^{-1}\partial_x v) = (1 - f^{-1}\partial_X v)^{-1}$, relative to the linear solution. We note that this relationship between linear and non-linear models has only been shown to be valid for the case of uniform interior PV, whereas here we have a variable PV. Nonetheless, here we apply these transformations to the linear model solution shown in figure 8c to obtain the ad-hoc non-linear solution shown in 8d. The ad-hoc solution captures some features of the fully non-linear numerical solution such as the location of the surface front and asymmetry of the vertical velocity field. However, as a result of the very large Rossby number at the front, the ad-hoc solution also exhibits a discontinuity in the buoyancy field at the surface front (down to a depth of about $40m$) and an associated infinity in the vertical velocity, implying that diffusion and other non-linear effects are important in arresting the collapse of the surface front. These large Rossby number dynamics are discussed in detail in Shakespeare and Taylor (2015).

a. Wave propagation and frequency spectra

As seen in previous sections, the spontaneously generated waves are horizontally trapped by the strain flow and rapidly become steady in the numerical solution (e.g. figure 7). This behavior is due to spatially uniform strain flow, and thus differs from what would be expected in the ocean where strain flows vary greatly in space (both horizontally and vertically). While we cannot directly represent such spatial variability in our simple quasi-2D model, we can capture some of the dynamics by considering a temporal variation in the spatially-uniform strain rate. In particular, here we consider switching off the strain flow in the steady numerical solutions described in the previous section (§3). As the strain rate is reduced, the trapped stationary waves are able to propagate, consistent with observations of waves at ocean fronts (e.g. Alford et al. 2013), and we can analyze the frequency spectrum of the flow and compare to our analytic predictions.

The methodology is as follows. We take the steady numerical solution (figure 7a) from the previous section and at time $t = 60$ hours switch off the strain flow in two ways: (a) instantaneously such that

$$\alpha(t) = \begin{cases} \alpha_0 \left(1 - e^{-\left(\frac{t}{\tau}\right)^2}\right) & t \leq 60 \\ 0 & t > 60 \end{cases}, \tag{33}$$

and (b) gradually over 60 hours such that

$$\alpha(t) = \begin{cases} \alpha_0 \left(1 - e^{-\left(\frac{t}{\tau}\right)^2}\right) & t \leq 60 \\ \alpha_0 \left(1 - e^{-\left(\frac{120-t}{\tau}\right)^2}\right) & 60 < t \leq 120 \\ 0 & t > 120 \end{cases}, \tag{34}$$

where time is in hours and the parameter values are the same as previously (i.e. $\tau = 2\pi/f$, $\alpha_0 = 0.4f$). The frequency spectrum of the vertical velocity field, $|\widehat{w}|(x,z,\omega)$, in each case is then analyzed for a period of 120 hours from when the strain rate reaches zero (this approach avoids

any Doppler shifting of the frequency due to non-zero background flow, e.g. (22e)). Here we will consider the spatially averaged vertical velocity spectrum (units: m) defined by

$$\langle|\widehat{w}|\rangle = \frac{\int\int|\widehat{w}|\,dx\,dz}{\int\int dx\,dz}. \tag{35}$$

The spectrum $\langle|\widehat{w}|\rangle$ is plotted in figure 9 for the (a) instantaneous and (b) gradual strain switch-off. Three spectra are shown in each plot: the average over the whole numerical domain (solid), the average above $50m$ (dashed), and the average below $4km$ (dotted). The global average in figure 9a shows three distinct spectral peaks coincident with the frequencies corresponding to the secondary circulation (vertical line labelled B), and the first two wave modes (vertical lines labelled C and D) for a strain rate of $0.4f$ as derived from figures 3 and 4. Thus, unsurprisingly, once the strain flow is switched off, the previously stationary wave modes begin to propagate at the frequency set by their slopes. The first wave mode (C) is particularly evident. Perhaps less expected is the strong wave generation corresponding to what we previously identified as the secondary circulation or frontal jets (line B; global spectra). This wave generation is associated with the 'adjustment' of the secondary circulation — that is, once the strain rate becomes zero, a steady secondary circulation cannot be supported at the front, and the excess momentum (sometimes called a 'momentum imbalance') is removed via the generation of inertia gravity waves. This adjustment generation has previously been examined in various contexts by many authors (e.g. Rossby 1938; Blumen 2000; Shakespeare and Taylor 2013, 2015). These adjustment waves would be generated even in the limit of very weak strain rate, if the strain field is turned off instantaneously, in contrast to the identified wave modes (C, D), which would vanish in this limit.

Now instead consider frequency spectrum associated with the gradual switch-off plotted in figure 9b. The gradual variation of the strain rate ensures that there is no instantaneous adjustment process, and the spectral peak associated with the secondary circulation is no longer present. In

addition, instead of distinct spectral peaks corresponding to individual wave modes (lines C, D), there is a broad band of high frequency wave energy which peaks around $2f$. The reason for this is that as the strain rate varies the resonant wave mode frequencies (e.g. figure 4) change, such that waves of different frequencies are continually being generated via the acceleration of the strain flow around the front. Notably, the peak spectral amplitude still occurs around $2f$ which agrees with the lowest frequency (highest amplitude) wave mode for strain rates in the range $0.25 < \alpha/f < 0.4$ (see figure 4). The globally averaged spectrum in figure 9b also exhibits a peak at the inertial frequency (line A) associated with direct forcing from the time-varying strain rate which itself varies near-inertially (e.g. (34)).

4. Discussion

Here we have investigated the spontaneous generation of inertia-gravity waves at strongly strained density fronts. In §2a we developed a linearized model to derive solutions for the circulation and density fields associated with a background strain flow, $\bar{U} = -\alpha x$, acting across a frontal buoyancy anomaly in a semi-infinite domain. The solutions depend only on the magnitude of the strain rate and the structure of the frontal anomaly, $b_0(x,z)$, at some instant in time. All information about the amplitude and structure of the frontal circulation, and wave Lagrangian frequencies, is contained with the Green's function for the problem (see figure 1). Whether waves are generated at a given front is determined by the Burger number of the front and the strain rate. Here we define the Burger number as $\varepsilon_F = NH/(fL)$, where H is the depth of the frontal structure, L the width, and N/f the ratio of buoyancy to inertial frequencies. Wave generation is predicted for Burger numbers exceeding about 0.5 and strain rates, α, exceeding about $0.2f$. The lowest frequency distinct wave predicted to be generated by the present mechanism has Lagrangian frequency $\omega = 1.93f$ and is generated for a strain rate of $\alpha = 0.29f$ (see figure 4). Based on these

results, it seems unlikely that the mechanism of wave generation examined here was responsible for the front-sourced waves observed by Alford et al. (2013) which were of very low frequency ($\sim 1.01f$). Wave amplitudes increase with increasing frontal Burger number and background strain rate.

We also investigated the mechanism responsible for the generation of the frontal waves. In §2b we showed that wave generation at a strained front is mathematically analogous to the classical scenario of 'lee wave' generation associated with a uniform flow over a topographic ridge in a rotating system (e.g. Queney 1947). Waves are generated in each case whenever the acceleration of the background flow around the front/ridge into the stratified ambient is fast enough that it forces the system away from geostrophic balance. More generally, any structure that presents an obstacle to the background strain flow will tend to generate waves, not only surface density fronts. Indeed, the analytic solution implies that any surface or interior PV anomaly q_0 (i.e. equation (5)) with some horizontal structure, whether in a bounded or unbounded domain, will generate waves in a strain flow. This result appears to be closely related to that of recent analytical studies describing the generation of gravity waves by a PV anomaly in a *shear* flow (Lott et al. 2010, 2012). These studies also employed a similar analytic approach using linearized equations of motion.

The present model is intended as a first-order description of wave generation in regions of the ocean with both sharp horizontal buoyancy gradients (order one frontal Burger numbers) and strong strain flows, such as the ocean submesoscale. Based on the analytic model results, we anticipate strong wave generation at submesoscale fronts. However, submesoscale fronts also typically exhibit large vorticity and Rossby number — a parameter that is assumed to be small in the linearized analytical model. Despite this assumption, in §3 we showed that the wave field in the analytic solution compares well with a fully non-linear numerical solution to the problem (i.e. equations (3)) for parameter values representative of a submesoscale front. The solutions

644 only differ significantly near the surface front, with the numerical solution developing an intense
645 downward jet on the cooler side of the front. The shallowest slope waves on the cooler side of
646 the front are also intensified relative to the analytic prediction, and tend to appear earlier than
647 their counterparts on the warm side. Given these relatively minor differences, we can be confident
648 that the analytic model provides a robust, first-order dynamical description of one mechanism of
649 inertia-gravity wave generation at strained density fronts.

650 However, more investigation is needed in more realistic models to quantify the relative impor-
651 tance of spontaneous generation at strained density fronts to the global wave field. The model
652 used herein is highly idealized, describing a two-dimensional front subject to a spatially uniform
653 background strain flow. These assumptions will almost certainly break down on the submesoscale
654 where both the background strain flows and the density fronts are highly three-dimensional in
655 character, and evolve on super-inertial timescales. For example, Nagai et al. (2015) use a high
656 resolution numerical model to show that spontaneous generated waves at fronts can be reabsorbed
657 by the mean flow, rather than propagating away as described by our model. More realistic spatial
658 and temporal variability will also likely modify the amplitude and frequencies of generated waves
659 compared to our analytic predictions. These effects will be studied in a future work.

660 *Acknowledgments.* CJS was supported by a Gates Cambridge Scholarship.

661 **References**

662 Alford, M. H., A. Y. Shcherbina, and M. C. Gregg, 2013: Observations of near-inertial internal
663 gravity waves radiating from a frontal jet. *J. Phys. Oceanogr.*, **43**, 1225–1239.

664 Blumen, W., 2000: Inertial oscillations and frontogenesis in a zero potential vorticity model. *J.*
665 *Phys. Oceanogr.*, **30**, 31–39.

Booker, J. R., and F. P. Bretherton, 1967: The critical layer for internal gravity waves in a shear flow. *J. Fluid Mech.*, **27 (03)**, 513–539.

Capet, X., J. C. McWilliams, M. J. Molemaker, and A. F. Shchepetkin, 2008: Mesoscale to submesoscale transition in the California Current system. Part II: Frontal processes. *J. Phys. Oceanogr.*, **38**, 44–64.

Danioux, E., J. Vanneste, P. Klein, and H. Sasaki, 2012: Spontaneous inertia-gravity-wave generation by surface-intensifed turbulence. *J. Fluid Mech.*, **699**, 153–1732.

D'Asaro, E., C. Lee, L. Rainville, R. Harcourt, and L. Thomas, 2011: Enhanced turbulence and energy dissipation at ocean fronts. *Science*, **332 (6027)**, 318–322.

Ford, R., 1994: The instability of an axisymmetric vortex with monotonic potential vorticity in rotating shallow water. *J. Fluid Mech.*, **280**, 303–334.

Gill, A. E., 1984: On the behavior of internal waves in the wakes of storms. *J. Phys. Oceanogr.*, **14 (7)**, 1129–1151.

Griffiths, M., and M. J. Reeder, 1996: Stratospheric inertia-gravity waves generated in a numerical model of frontogenesis. I: Model solutions. *Q. J. Roy. Meteor. Soc.*, **122**, 1153–1174.

Gula, J., M. J. Molemaker, and J. C. McWilliams, 2014: Submesoscale cold filaments in the Gulf Stream. *J. Phys. Oceanogr.*, **44 (10)**, 2617–2643.

Hosegood, P. J., M. C. Gregg, and M. H. Alford, 2013: Wind-driven submesoscale subduction at the north Pacific subtropical front. *J. Geophys. Res.*, **118 (10)**, 5333–5352.

Hoskins, B. J., and F. P. Bretherton, 1972: Atmospheric frontogenesis models: mathematical formulation and solution. *J. Atmos. Sci.*, **29**, 11–37.

687 Kunze, E., 1985: Near-inertial wave propagation in geostrophic shear. *Journal of Physical*
688 *Oceanography*, **15 (5)**, 544–565.

689 Lott, F., R. Plougonven, and J. Vanneste, 2010: Gravity waves generated by sheared potential
690 vorticity anomalies. *J. Atmos. Sci.*, **67 (1)**, 157–170.

691 Lott, F., R. Plougonven, and J. Vanneste, 2012: Gravity waves generated by sheared three-
692 dimensional potential vorticity anomalies. *J. Atmos. Sci.*, **69 (7)**, 2134–2151.

693 Mahadevan, A., and A. Tandon, 2006: An analysis of the mechanisms for submesoscale vertical
694 motion at ocean fronts. *Ocean Modell.*, **14**, 241–256.

695 Marshall, J., A. Adcroft, C. Hill, L. Perelman, and C. Heisey, 1997: A finite-volume, incom-
696 pressible Navier Stokes model for studies of the ocean on parallel computers. *J. Geophys. Res.*,
697 **102 (C3)**, 5753–5766.

698 Muraki, D. J., 2011: Large-amplitude topographic waves in 2D stratified flow. *J. Fluid Mech.*,
699 **681**, 173–192.

700 Nagai, T., A. Tandon, E. Kunze, and A. Mahadevan, 2015: Spontaneous generation of near-inertial
701 waves by the Kuroshio Front. *J. Phys. Oceanogr.*, **45 (9)**, 2381–2406.

702 Pierrehumbert, R. T., 1984: Linear results on the barrier effects of mesoscale mountains. *J. Atmos.*
703 *Sci.*, **41 (8)**, 1356–1367.

704 Plougonven, R., and C. Snyder, 2005: Gravity waves excited by jets: propagation versus genera-
705 tion. *Geophys. Res. Lett.*, **32**, doi:10.1029/2005GL023730.

706 Plougonven, R., and F. Zhang, 2014: Internal gravity waves from atmospheric jets and fronts. *Rev.*
707 *Geophys.*, **52 (1)**, 33–76.

Polzin, K. L., and Y. V. Lvov, 2011: Toward regional characterizations of the oceanic internal wavefield. *Rev. Geophys.*, **49 (4)**.

Queney, P., 1947: *Theory of perturbations in stratified currents with applications to air flow over mountain barriers*. University of Chicago Press.

Reeder, M. J., and M. Griffiths, 1996: Stratospheric inertia-gravity waves generated in a numerical model of frontogenesis. II: Wave sources, generation mechanisms and momentum fluxes. *Q. J. Roy. Meteor. Soc.*, **122**, 1175–1195.

Rossby, C. G., 1938: On the mutual adjustment of pressure and velocity distributions in certain simple current systems, II. *J. Mar. Res.*, **1**, 239–263.

Rosso, I., A. M. Hogg, A. E. Kiss, and B. Gayen, 2015: Topographic influence on submesoscale dynamics in the Southern Ocean. *Geophys. Res. Lett.*, **42 (4)**, 1139–1147, doi: 10.1002/2014GL062720.

Rudnick, D. L., and J. R. Luyten, 1996: Intensive surveys of the Azores Front 1. Tracers and dynamics. *J. Geophys. Res.*, **101 (C1)**, 923–939.

Shakespeare, C. J., 2015a: Non-hydrostatic wave generation at strained fronts. *J. Atmos. Sci.*, **in press**.

Shakespeare, C. J., 2015b: On the generation of waves during frontogenesis. University of Cambridge.

Shakespeare, C. J., and J. R. Taylor, 2013: A generalized mathematical model of geostrophic adjustment and frontogenesis: uniform potential vorticity. *J. Fluid Mech.*, **736**, 366–413.

Shakespeare, C. J., and J. R. Taylor, 2014: The spontaneous generation of inertia-gravity waves during frontogenesis forced by large strain: theory. *J. Fluid Mech.*, **757**, 817–853.

730 Shakespeare, C. J., and J. R. Taylor, 2015: The spontaneous generation of inertia-gravity waves
731 during frontogenesis forced by large strain: numerical solutions. *J. Fluid Mech.*, **accepted**.

732 Shcherbina, A. Y., E. A. D'Asaro, C. M. Lee, J. M. Klymak, M. J. Molemaker, and J. C.
733 McWilliams, 2013: Statistics of vertical vorticity, divergence, and strain in a developed sub-
734 mesoscale turbulence field. *Geophys. Res. Lett.*, **40**, doi:10.1002/grl.50919.

735 Snyder, C., W. Skamarock, and R. Rotunno, 1993: Frontal dynamics near and following frontal
736 collapse. *J. Atmos. Sci.*, **50**, 3194–3211.

737 Thomas, L. N., 2012: On the effects of frontogenetic strain on symmetric instability and inertia-
738 gravity waves. *J. Fluid Mech.*, **711**, 620–640.

739 Thomas, L. N., A. Tandon, and A. Mahadevan, 2008: Submesoscale processes and dynamics.
740 *Geophysical Monograph Series 177: Ocean Modeling in an Eddying Regime*, American Geo-
741 physical Union.

742 Vanneste, J., 2013: Balance and spontaneous wave generation in geophysical flows. *Annu. Rev.*
743 *Fluid Mech.*, **45**, 147–172.

744 Viudez, A., and D. G. Dritschel, 2006: Spontaneous generation of inertia-gravity wave packets by
745 balanced geophysical flows. *J. Fluid Mech.*, **553**, 107–117.

746 Whitt, D. B., and L. N. Thomas, 2013: Near-inertial waves in strongly baroclinic currents. *Journal*
747 *of Physical Oceanography*, **43 (4)**, 706–725.

748 Williams, R. T., and J. Plotkin, 1968: Quasi-geostrophic frontogenesis. *J. Atmos. Sci.*, **25**, 201–
749 206.

750 Wunsch, C., and R. Ferrari, 2004: Vertical mixing, energy and the general circulation of the
751 oceans. *Annu. Rev. Fluid Mech.*, **36**, 281–314.

Zhang, F., 2004: Generation of mesoscale gravity waves in upper-tropospheric jet-front systems. *J. Atmos. Sci.*, **61**, 440–457.

LIST OF FIGURES

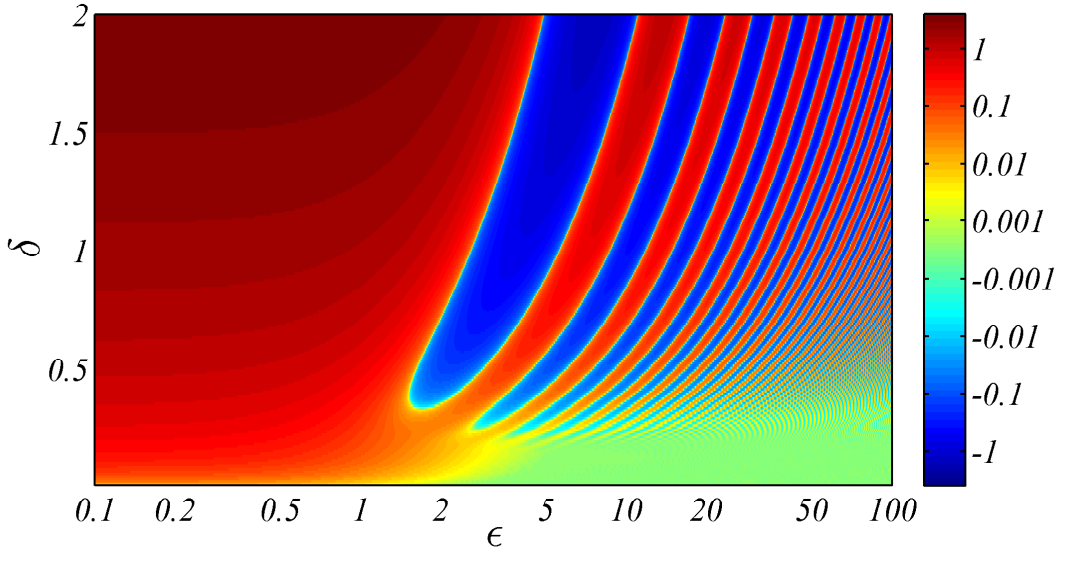

FIG. 1. Non-dimensional Green's function for the cross-front shear, $f\widehat{\partial_z u_G}$ (17), as a function of slope $\varepsilon = Nk/(fm)$ and strain rate $\delta = \alpha/f$. Local extrema in the Green's function correspond to waves (resonant modes) with Lagrangian frequency $\omega = f\sqrt{1+\varepsilon^2}$.

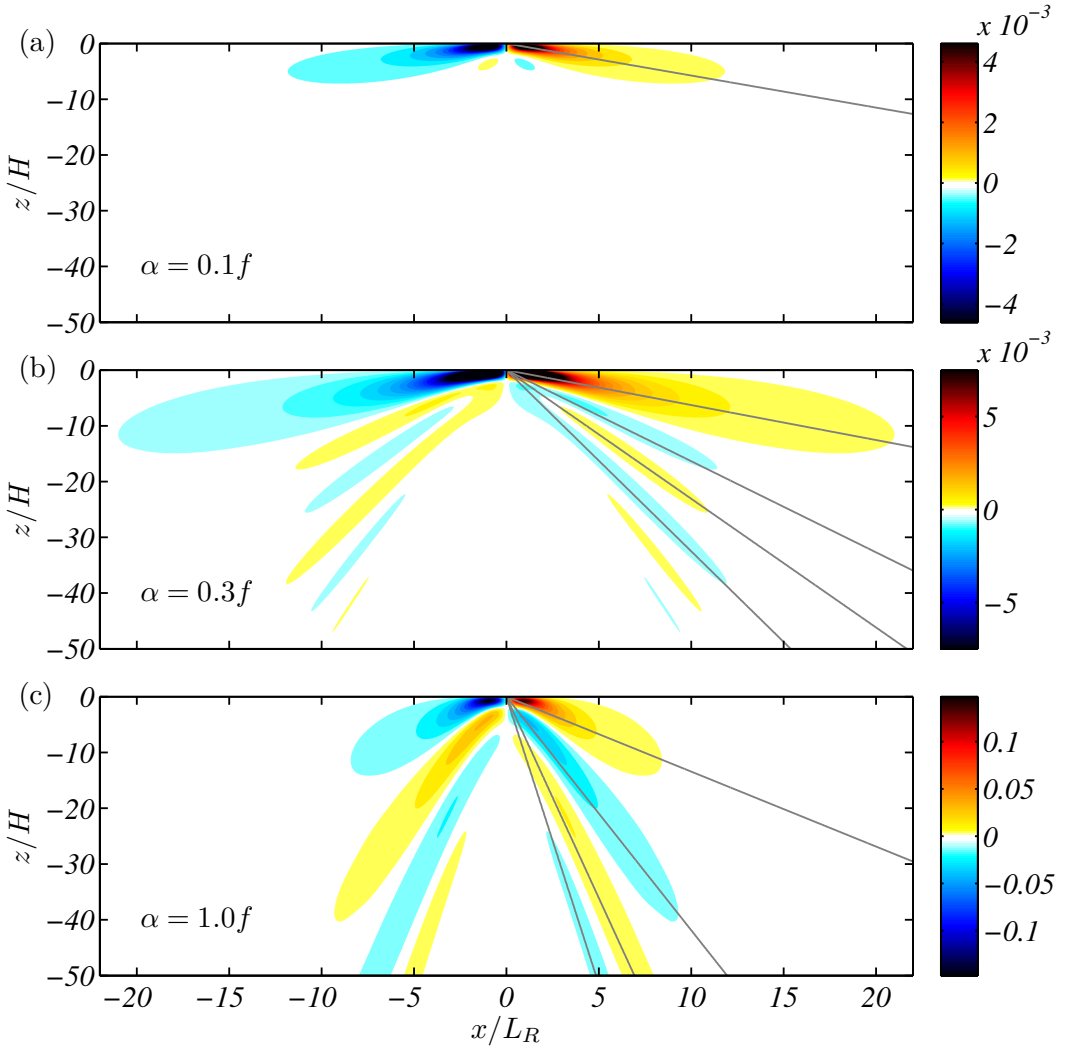

FIG. 2. Comparison of vertical velocity field (in units of $\Delta b_0 f/N^2$) for strain rates (a) $\alpha = 0.1f$, (b) $\alpha = 0.3f$, and (c) $\alpha = f$, and a frontal anomaly defined by (21). Straight grey lines indicate the slopes of secondary circulation and first three wave modes (if they exist), as predicted from the Green's function (see figures 3 and 4).

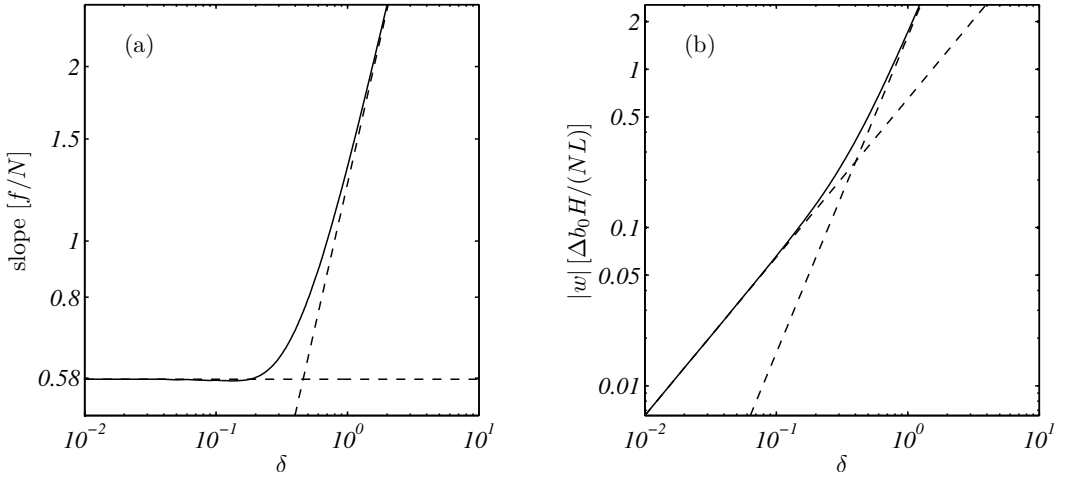

FIG. 3. (a) Slope of the frontal jets as a function of strain rate, in units of f/N. (b) Vertical velocity magnitude as a function of strain rate, in units of $\Delta b_0 H/(NL)$. The results from the small (19) and large (20) strain rate limits are shown as dashed lines. The slope is nearly constant at small strain rate and increases linearly at large strain rate. The vertical velocity increases linearly at small strain rate and quadratically at large strain rate.

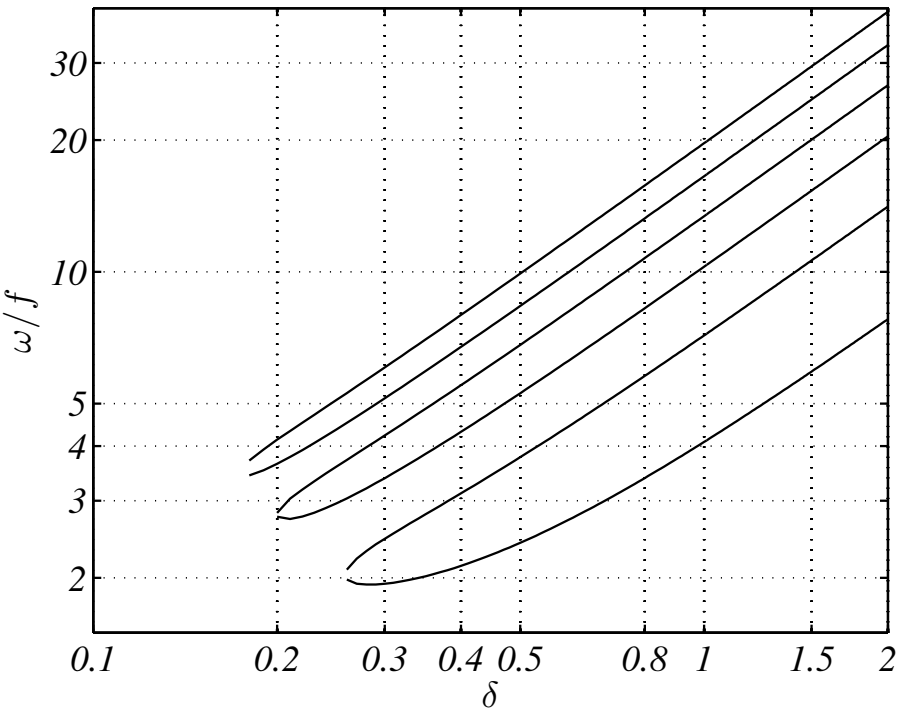

FIG. 4. Frequencies of the six lowest frequency distinct wavepackets as a function of strain rate $\delta = \alpha/f$, derived from computing the local extrema of the non-dimensional cross-front shear Green's function, $f\widehat{\partial_z u_G}$, shown in figure 1. The lowest Lagrangian frequency associated with a distinct wave mode is $\omega = 1.93f$, for a strain rate of $\alpha = 0.29f$.

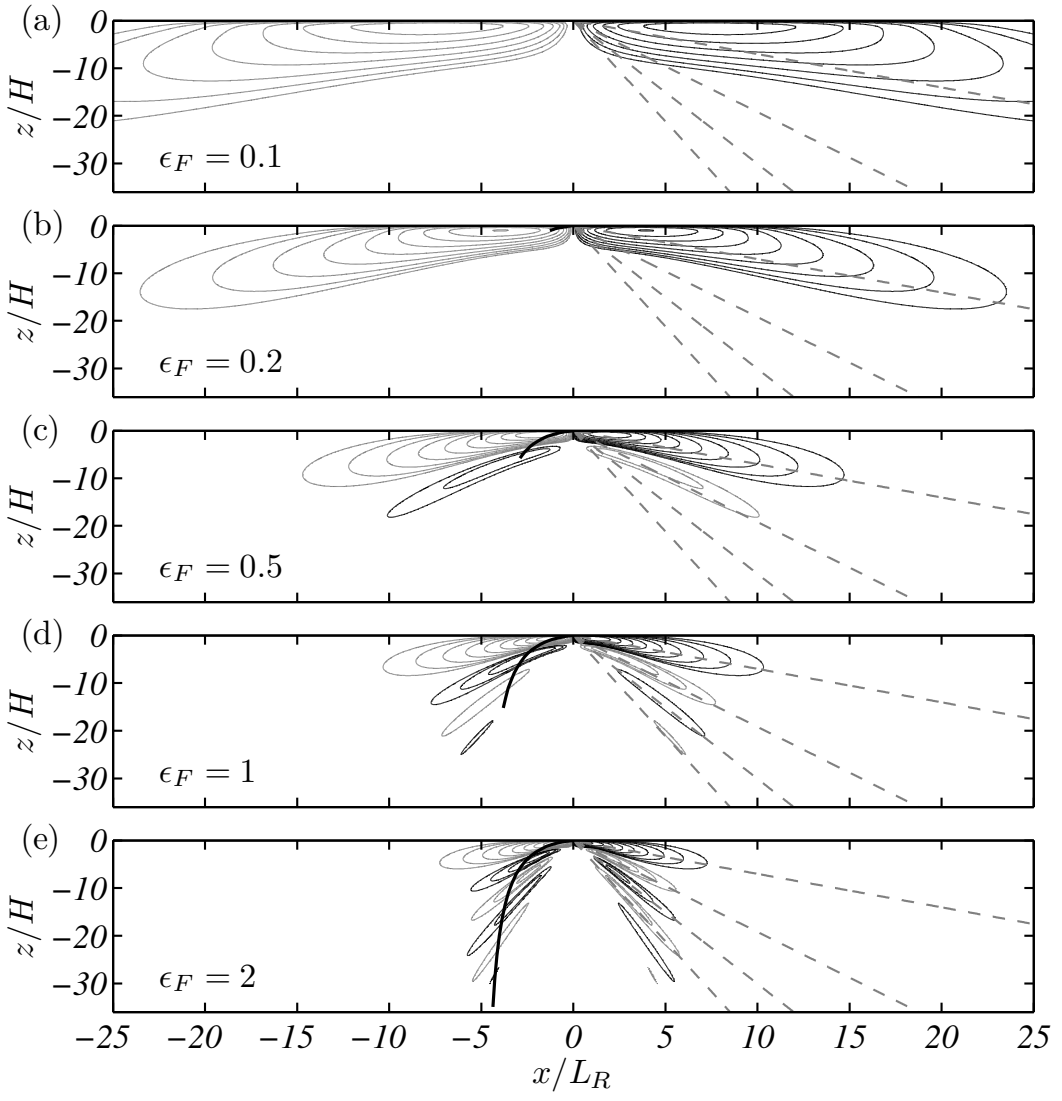

FIG. 5. Vertical velocity fields for a strain rate of $\alpha = 0.4f$ and buoyancy anomaly defined by (21), for various frontal Burger numbers $\epsilon_F = L_R/L$. The velocities are in units of $\epsilon_F \Delta b_0 f/N^2$. Contours are logarithmically spaced from 3 to 100% of the maximum value (0.03). Grey-dashed lines indicate the predicted slope of the frontal jets and waves. The figure can also be viewed as a sequence of snapshots in time, $\alpha t = \ln(\epsilon_F/0.1)$: (a) $\alpha t = 0$, (b) $\alpha t = 0.69$, (c) $\alpha t = 1.61$, (d) $\alpha t = 2.30$, and (e) $\alpha t = 3$. The path of a wave packet initially located at the origin at $t = 0$, with initial wavenumbers $k_0 = 0.2/L_R$ and $m_0 = 0.5/H$, is shown by a solid black line on each plot. The terminus of the line is the position of the wave packet at the time the snapshot is taken. Note that the velocities have been non-dimensionalised by $\epsilon_F \Delta b_0 f/N^2$, such that the maximum velocity in (e) is 20 times that in (a) owing to the change in ϵ_F.

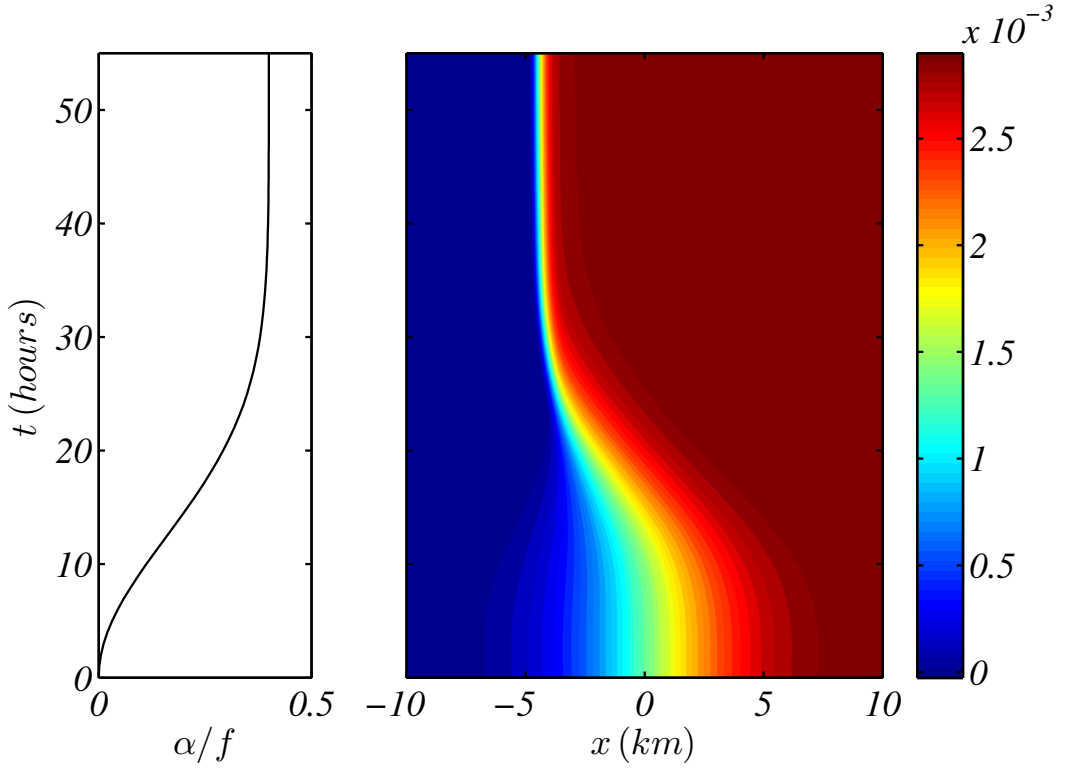

826 FIG. 6. The time evolution of the strain rate, $\alpha(t)/f$, and the surface buoyancy field, $b(x,0,t)$, in the numerical
827 model. A steady state is reached after about 45 hours.

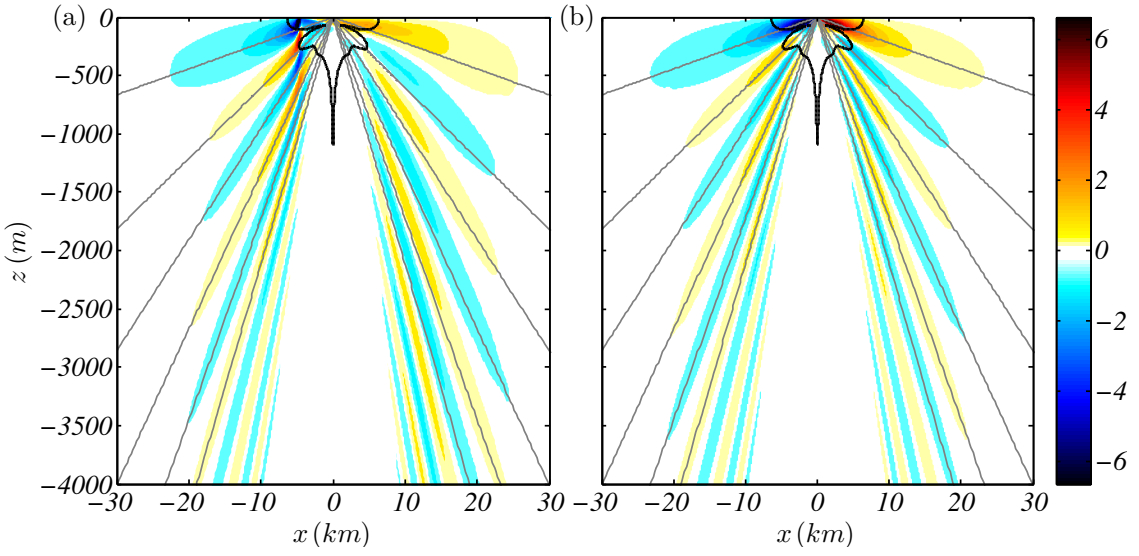

828 FIG. 7. Comparison of the numerical and analytical solutions. (a) The steady state numerical vertical velocity
829 (m day^{-1}) field. (b) The analytical vertical velocity field (m day^{-1}) for the same frontal structure (see text for
830 details). The grey lines on each plot are the wave and jet slopes predicted from the Green's function. The region
831 for which $|u| > 0.1|\bar{U}|$, where the analytical model is expected to break down, is enclosed by a solid black line
832 on each plot.

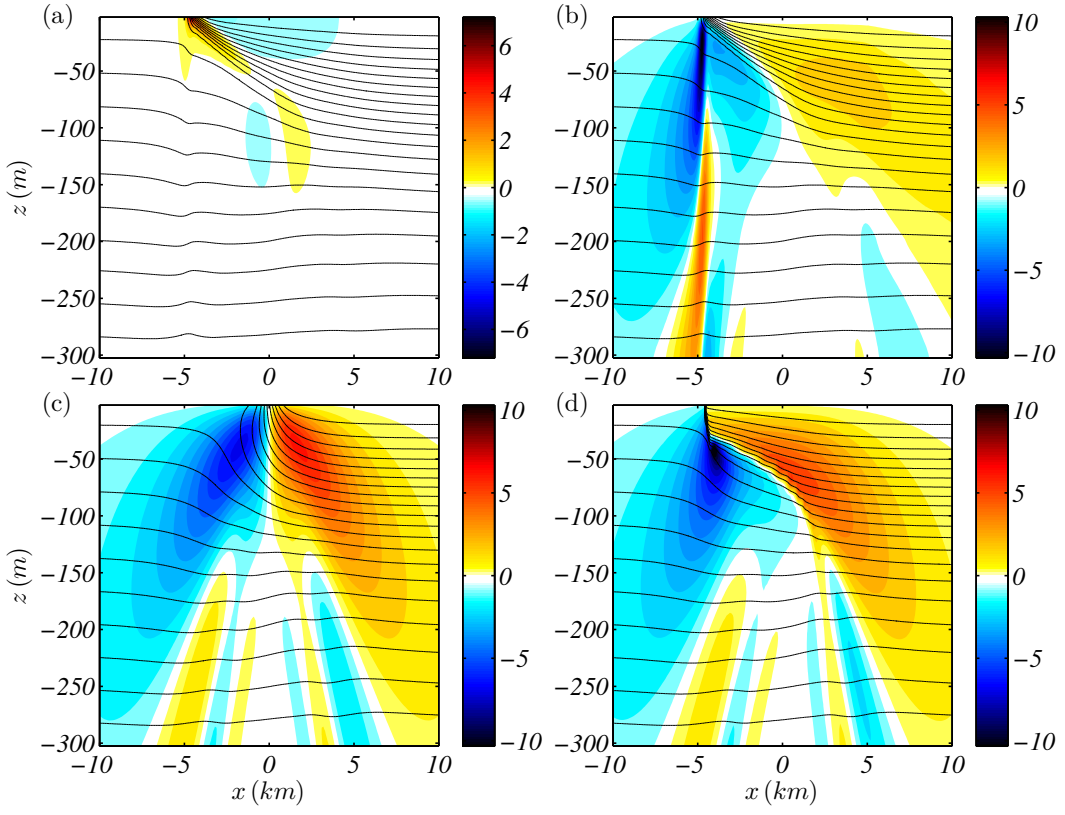

FIG. 8. Comparison of the numerical and analytical solutions near the surface front. (a) The vorticity Rossby number $Ro = f^{-1}\partial_x v$ in the numerical model steady state. (b) The vertical velocity field (m day^{-1}) and buoyancy contours in the numerical model steady state. (c) The vertical velocity field (m day^{-1}) and buoyancy contours predicted by the analytical model. (d) The vertical velocity field (m day^{-1}) and buoyancy contours of the ad-hoc non-linear analytical model (see text for detailed description).

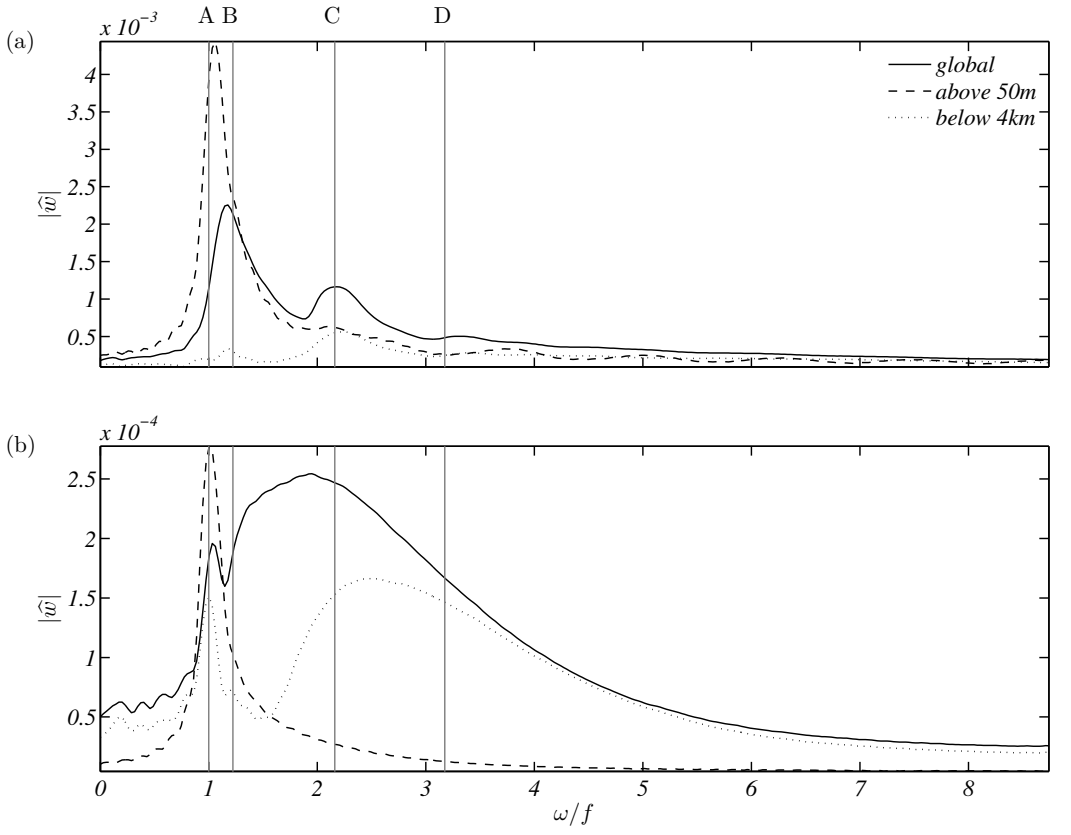

FIG. 9. Spatially averaged vertical velocity frequency spectra $\langle|\widehat{w}|\rangle$ (m) from the numerical solution when the strain is turned off (a) instantaneously (33) and (b) gradually (34). Three lines are displayed on each plot for the global average spectrum (solid), near-surface spectrum (above 50m, dash) and deep spectrum (below 4km, dotted). The vertical grey lines labelled A to D indicate the specific frequencies of interest: A = inertial frequency, B = secondary circulation 'frequency', C = first wave mode frequency, and D = second wave mode frequency, as predicted from the constant strain analytic model for a strain rate of $\alpha = 0.4f$.